High-resolution back-projection at regional distance: application to the Haiti M7.0 earthquake and comparisons with finite source studies

L. Meng[1], J.-P. Ampuero[1], A. Sladen[2] and H. Rendon[3]

1. Seismological Laboratory, California Institute of Technology

2. CNRS - Géoazur, Univ. de Nice-Sophia Antipolis

3. Fundación Venezolana de Investigaciones Sismológicas

Abstract:

A catastrophic Mw 7 earthquake ruptured on January 12th 2010 on a complex fault system near Port-au-Prince, Haiti. Offshore rupture is suggested by aftershock locations and marine geophysics studies but its extent remains difficult to define using geodetic and teleseismic observations. Here we perform the multi-taper MUSIC analysis, a high resolution array technique, at regional distance with recordings from the Venezuela National Seismic Network to resolve high frequency (about 0.4 Hz) aspects of the earthquake process. Our results indicate westward rupture with two subevents, roughly 35 km apart. In comparison, a lower frequency joint finite source inversion, with fault geometry based on new geologic and aftershock data, shows two slip patches with centroids 21 km apart. Apparent source time functions obtained from USArray further constrain the inter-subevent time delay, which implies a rupture speed of 3.3 km/s. The tips of the slip zones coincide with the subevents imaged by back-projections. The different subevent locations found by back-projection and by source inversion suggest spatial complementarity between high and low frequency source radiation, consistent with high frequency radiation originating from rupture arrest phases at the edges of main slip areas. The GCMT solution and a geodetic-only

inversion have similar moment, indicating most of the moment release is captured by geodetic observations without requiring additional rupture offshore. Our results demonstrate the contribution of source imaging by back-projections of regional seismic array data for earthquakes down to M≈7, especially when incomplete coverage of seismic and geodetic data imply large uncertainties in source inversions.

1. Introduction

The M7 earthquake that hit Haiti in January 2010 was one of the most devastating natural disasters of the last decades. The disproportionate damage caused by this event and the prospect of future hazards in the region have prompted efforts to better understand its rupture process and the tectonics of the Northeast Caribbean, in particular the Enriquillo-Plantain-Garden Fault (EPGF) and the surrounding fault systems. [*Nettles and Hjorleifsdottir*, 2010] found that a composite source model with a strike-slip sub-event followed by a smaller thrust sub-event was consistent with long-period teleseismic data. Using geodetic data, [*Calais et al.*, 2010; *Hashimoto et al.*, 2011] attributed the slip to two asperities on a previously unmapped fault in the Leogane delta, north from the EPGF. Based on the analysis of geodetic, geologic and teleseismic observations [*Hayes et al.*, 2010] also inferred rupture primarily on the blind Leogane fault, with a minor contribution on the EPGF. One of the outstanding uncertainties about this event is the extent of its rupture in offshore areas that are poorly constrained by on-land geodetic data. The possibility of coseismic slip offshore is suggested by active deformation identified by a marine geophysical survey and by the location of aftershocks derived from a combined temporary seismic network of 4 land and 21 ocean bottom stations (Haiti-OBS campaign) [*Mercier de Lépinay et al.*, 2011].

While finite fault inversions provide possible source models, they rely on a priori information about the fault geometry, which is not readily available for the Haiti event due to the geological complexity of the fault system and to the lack of surface rupture [*Prentice et al.*, 2010] and strong motion recordings. In addition, the source inversion problem suffers from limited resolution of the spatio-temporal rupture process due to its low frequency band. Source imaging by back-projection of body waves recorded by dense arrays allows to track the areas of strongest high frequency radiation [*Ishii et al.*, 2005; *Fletcher et al.*, 2006; *Vallee et al.*, 2008]. This technique constrains the spatio-temporal properties of the rupture (length, direction, speed, segmentation) based solely on the phase of coherent seismic array signals. It does not rely on detailed knowledge of Green's functions and fault geometry, on restrictive parameterizations of the rupture kinematics, nor on additional smoothing. The high frequency aspects of the rupture process imaged by array back-projection are complementary to traditional finite source inversion models based on teleseismic and geodetic data, which are instead sensitive to low frequencies and to the static field. Conventionally, back-projection is applied to large seismic arrays at teleseismic distances [*Ishii et al.*, 2005; *Meng et al.*, 2011] or to small aperture strong-motion arrays at local distances [*Spudich and Cranswick*, 1984; *Fletcher et al.*, 2006]. Seismic arrays at regional distances can provide higher aperture to distance ratio and thus higher resolution. [*Vallee et al.*, 2008] exploited surface waves recorded by a regional array to study the 2001 Mw 7.8 Kunlun earthquake over a frequency band (0.04 to 0.1 Hz) adequate to study very long ruptures, but too low to resolve smaller earthquakes. In principle, higher frequency body waves carry higher resolution information. However, the complexity of regional Pn waves has prevented seismologists from fully exploiting this phase for source imaging. Earthquake source studies using regional body wave phases have been mainly limited to inferring macroscopic source properties from recordings at distances up to a few hundred km [*Zhu and Helmberger*, 1996; *Mendoza*, 2005; *Wei et al.*, 2009]. [*Guilbert et al.*, 2005] imaged the rupture propagation of a very large event, the 2004 Mw 9.0 Sumatra earthquake, by array processing of body waves recorded by the CMAR-seismic array at regional distance. Here, we further show that the relatively sustained character of the Pn phase enables the application of high resolution array processing techniques on moderate earthquakes (M≈7) to provide complementary constraints on rupture length and locations of high-frequency source radiation. This capability can contribute to rapid hazard and damage assessment for future earthquakes in the Caribbean region. The rest of this article is organized as follows. In section 2 we describe the data recorded by Venezuela National Seismic Network and argue for the need of high resolution regional array analysis. In section 3 we present a high resolution array source imaging technique adapted to earthquakes recorded at regional distance and quantify the resolution of the technique through extensive synthetic tests. In section 4 we present our results of source imaging of the Haiti earthquake by regional array analysis. In section 5 we integrate these results with independent analysis of apparent source time functions and rupture speed based on USArray data and an improved finite fault model based on teleseismic and geodetic data. In section 6 we discuss the frequency dependent source properties, the possibility of offshore coseismic rupture and the potential contribution of regional arrays to earthquake studies.

2. VNSN data, pre-processing and selection

Our array back-projection study of the 2010 Haiti event is based on data recorded at regional distance by the Venezuela National Seismic Network (VNSN). The VNSN is composed of 22 broad-band stations, oriented mainly East-West, located approximately 9.5 degrees from Haiti in the perpendicular direction to the EPGF strike (Fig.1). The VNSN has a privileged geometrical configuration and location to study large earthquake ruptures in the Caribbean region.

Array processing at regional distance aims at estimating the azimuth of arrival and relative timing of the seismic phases radiated from the strongest subevents of the earthquake.The study of the 2010 Haiti earthquake remains challenging because of its compact source size, shorter than 40 km according to previous studies [*Calais et al.*, 2010; *Hayes et al.*, 2010]. The resolution length scale along the fault that can be achieved with the standard beamforming techniques is evaluated by the array response function [*Rost and Thomas*, 2002]. Figure 2 shows the array response of the VNSN and the USArray, the nearest array at teleseismic distance. The array responses are back-projected into the hypocentral region of the 2010 Haiti earthquake based on P travel times computed by the Tau-P toolkit and the IASP91 model. The array response of VNSN is not isotropic. It has low resolution along the range direction (the source-to-array direction) but adequate cross-range resolution (sub parallel to the fault strike in this case). In regional array processing, the range resolution is considerably poorer than the cross-range resolution, due to the small variability of the slowness of Pn waves as a function of epicentral distance. Hence, hereafter we map the array analysis results onto the fault plane by projecting them along the major axis of the array response pattern. The along-strike resolution length achieved by the USArray is approximately twice of that of the VNSN due to its more distant location and its more unfavorable orientation with respect to the fault strike. We note that the array response provides an ideal estimate of the array resolution. In practice, resolution is further affected by waveform incoherence and interference, as discussed through synthetic tests in section 3.2. Thus, to achieve adequate imaging of the Haiti earthquake the back-projection requires data from an array at regional distance. Moreover, since previous studies indicate that the rupture length of the Haiti earthquake is as compact as 40 km, the analysis requires an array processing technique that can achieve higher resolution than standard beamforming.

The Pn waveforms recorded by the VNSN are filtered between 0.2 and 0.7 Hz. The low frequency cutoff is dictated by a time-frequency trade-off (see section 3.1). The high frequency cutoff is determined by the coherency of the array data, which is ultimately determined by the spacing between stations. The dominant frequency of the Pn waves is about 0.4 Hz. We align the waveforms on their first arrival by multi-channel alignment [*Vandecar and Crosson*, 1990] based on cross-correlation of 10 seconds long windows containing the first Pn arrivals. This procedure reduces the effect of travel time errors due to uncertainties in the velocity structure e.g. [*Ishii et al.*, 2005].

Array processing techniques assume coherent signals across the array. We select a subset of 13 stations with adequate waveform coherency by inspecting the array data coherence matrix. This matrix is made of the coherence between all pairs of stations computed during the multi-channel alignment procedure. The indices of the matrix are reordered to group together the most mutually coherent stations (Fig. 3). We found a modified k-nearest neighbors clustering algorithm (www.eigenvector.com/MATLAB/Mac_Mfiles/corrmap.m) to be adequate for this purpose. After inspection of the reordered matrix we select a subset of 13 stations that consistently have correlation coefficients larger than 0.8 (Fig.3).

3. High resolution multi-taper/MUSIC technique for regional arrays

3.1. Outline of the method and parameter settings

Here, we apply at regional distance a high-resolution array analysis technique originally developed for a teleseismic array study [*Meng et al.*, 2011]. The method combines the Multiple Signal Classification (MUSIC) array processing technique [*Schmidt*, 1986; *Goldstein and Archuleta*, 1991; *Guilbert et al.*, 2005] with multi-taper cross-spectrum estimation [*Thomson*, 1982]. MUSIC was designed for high resolution direction of arrival estimation of long and stationary signals [*Krim and Viberg*, 1996]. The Pn phase is relatively stationary. The multi-taper method yields a robust estimate of the data coherence matrix on relatively short time window and thus improves significantly the temporal resolution of MUSIC. Here we only describe the choice of processing parameters for this particular study. More details about the method are described by [*Meng et al.*, 2011].

Number of tapers in cross-spectrum estimation

The multi-taper technique [*Thomson*, 1982] averages multiple, almost independent cross-spectral estimates obtained after tapering the data by a sequence of orthogonal functions with optimal temporal and spectral concentration. These Slepian tapers are the set of functions of finite temporal duration T with maximum energy within the band of frequencies lower than the bandwidth W. Given a time window duration T and a frequency bandwidth W, the proper number of tapers is 2×T×W-1. As a compromise between useful averaging (large T×W) and adequate temporal resolution (short T) we use here 3 tapers, which implies $T \times W=2$.

Length of analysis window

The MUSIC method requires narrow band estimates of cross-spectrum, i.e. the bandwidth W (the frequency smearing of the spectral estimator) has to be small compared to any frequency of analysis, $W \ll f$. This implies a trade-off between temporal resolution and frequency localization: $T \times f \gg 2$ for 3 tapers. As a compromise here we set T=30 s, which satisfies $T \times f > 6$ for frequencies higher than 0.2 Hz. At the dominant frequency of our data, $f \approx 0.4$ Hz, we get $T \times f \approx 12$.

Number of principal eigenvalues

In MUSIC the signal subspace is defined as the subspace spanned by the distinctly largest eigenvalues of the data covariance matrix. Its complement defines the noise subspace. For stationary signals, the dimension N of the signal subspace is equal to the number of signal sources contributing to the data time window. In the case of transient seismic signals analyzed with relatively short time windows, each covariance matrix estimated with a separate taper tends to have only one non-zero eigenvalue and the associated eigenvectors tend to be independent. Hence, the rank of the covariance matrix obtained by linear combination of the multiple taper estimates tends to be equal to the number of tapers. In particular, the number of significant eigenvalues is at most three when using three tapers. Fig. 4 shows results of the MUSIC analysis of the 2010 Haiti earthquake at 0.4 Hz, the dominant frequency of the seismograms, with N ranging from 1 to 4. The MUSIC pseudo-spectrum, a measure of the orthogonality between the array steering vector associated to a candidate source location and the noise sub-space (for details see [*Meng et al.*, 2011]), is plotted as a function of along-strike position with respect to the hypocenter and as a function of end time of the sliding windows. The MUSIC pseudo-spectrum is normalized by its maximum in each time window. Its amplitude depends on signal power, coherence and interference but it does not directly represent any physical quantity. Nevertheless, the sharp peaks of the MUSIC pseudo-spectrum indicate the location of signal sources. In the MUSIC analysis of the Haiti earthquake, two main subevents (black dots in Fig. 4b) are visible and their estimated locations are independent of the choice of N. However, when N is too small (N=1) the analysis fails to resolve two simultaneous sources, it only indicates the strongest source in each time window. The results with N=2 or 3 show stable features of the rupture process including simultaneous multiple sources. When N is larger than the number of non-zero eigenvalues (e.g. N=4), the signal subspace is contaminated by noise and the resulting image is not stable. While the spatial location of the subevents is independent of the choice of N, their estimated timing is not. Because we have not developed yet a complete understanding of the effect of N on the timing of subevents, an objective rationale for the choice of N is not available at this time. Here we choose N=2 because it yields the most clear image of the westward rupture front and the resulting rupture speed is within the usual range, consistent with independent observations available for this earthquake, as described in later sections. We note, however, that the temporal details of the back projection images, which depend on N, are not used as additional constraints in our analysis of this earthquake.

3.2. Resolution tests

Synthetic test for an ideally coherent linear array

Fig. 5 compares the resolution of four techniques on synthetic transient signals: beamforming, cubic root stacking (a popular modification of beamforming, e.g. [*Rost and Thomas*, 2002]), correlation stacking and MUSIC. In correlation stacking the normalized cross-correlation coefficients are beamformed instead of the waveforms [*Fletcher et al.*, 2006] to improve robustness against scattering, multipathing and contamination by coda waves [*Borcea et al.*, 2005]. The color scale in the images by correlation stacking and cubic root stacking indicate beamformed cross-correlation coefficients and beamformed cubic root of the signal amplitude, respectively, evaluated or integrated over a sliding time window of duration 30 s The resolution of a method is defined as its ability to separate closely spaced sources. We consider two identical Pn plane waves with dominant frequency of 0.3 Hz impinging simultaneously but with different azimuth on a linear array of 21 sensors regularly spaced at half wavelength. Gaussian white noise is added with a signal to noise ratio of 10 dB. The results as a function of the relative azimuth between the two waves (Fig. 5) show that, the minimum azimuthal separation resolvable by beamforming, cubic root stacking, correlation stacking and MUSIC is approximately 8, 8, 6 and 3 degrees, respectively. This shows that, under perfect waveform coherency, the azimuthal resolution, and hence the spatial resolution in the cross-range direction, achieved by our multitaper MUSIC method achieves azimuthal resolution that outperforms the other methods by at least a factor of two.

Synthetic test for the VNSN array geometry

Fig. 6 shows further synthetic tests to understand the performance and potential bias of the back projection of the Haiti earthquake source using the VNSN data. We compute full wave field synthetics (Fig.7a) using the SPECFEM3D package [*Tromp* *et al.*, 2008] with the 3D crustal velocity model Crust2.0 [*Bassin et al.*, 2000]. Our simulations are accurate up to 0.33 Hz. Given the uncertainties in the velocity model, generating higher frequency synthetics is not warranted. Inspired by the final result of the back-projection, we test scenarios with a source containing two asperities. The first one is located at the hypocenter of the Haiti earthquake. The second one is located westward along the hypothetical Leogane fault trace [*Hayes et al.*, 2010]. We consider either the same slip amplitude for both subevents or a 2:1 ratio based on the source time functions estimated at the USArray (see section 5.1). We explore inter-subevent distances up to 50km, with rupture time delays consistent with a rupture speed of 3 km/s. For both asperities we assume source parameters from the CMT solution (focal mechanism 251/70/28, strike/dip/rake, and centroid depth 12 km) and a Brune source time function with duration of 3 seconds. In Fig.6, the left two columns show examples of cubic root stacking, correlation stacking and MUSIC pseudo-spectra. These quantities are back-projected onto the source area based on P travel times computed by the Tau-P toolkit and the IASP91 model.

We found that all the back-projection methods are modulated by interference between subevents. This introduces an amplitude and location fluctuation that depends periodically on the product of inter-subevent time delay and frequency of analysis. Fig. 8 shows two examples of interference in the cubic root stacking analysis at 0.3 Hz, with sources separated by 15 and 40 km respectively. The time delay between the wave arrivals from the two asperities varies across the array. Destructive interference occurs at stations where the waves from the two asperities are out of phase with respect to the dominant period (the seismograms of some stations are deficient in low frequencies in Fig. 8). This issue might be less severe in practice, since the synthetics are computed from two point sources. In reality, the broader slip region reduces the simultaneous destructive interference.

As expected from the resolution test, MUSIC achieves a smaller resolvable distance than the other two techniques. This difference is particularly prominent when we set a more realistic 2:1 amplitude ratio for the two sources. The left two columns in Figure 6 show the two snapshots taken at the beginning of each source (t=0s and t=10s) when d=30 km. The MUSIC pseudo-spectrum clearly gives two peaks in the second snapshot, while the other two techniques fail to resolve them. Note that the absolute amplitude of the MUSIC pseudo-spectrum, which is modulated by interference patterns, does not directly represent the signal power and is not used in the analysis. The resolution limit for MUSIC in these synthetic tests is approximately 25 km with an uncertainty of about 5 km for each sub-source. Considering the uncertainty is mainly introduced by the interference effect, which is less prominent in practice, 5 km is regarded as the upper bound of the relative location uncertainty in our analysis.

4. Results of array analysis of the 2010 Haiti earthquake at regional distance

We first illustrate the accuracy of our method by an analysis of the largest aftershock, a M 5.9 (NEIC) earthquake on January 20th 2010 (waveform shown in Fig.7b). The back-projection of the MUSIC pseudo-spectrum into the source region is shown in map view in the first two columns of Fig. 9d for two windows ending at t=15 s and 30 s after the first arrival, respectively. The warmest color indicates the location of the source of the waves arriving at the VNSN within these time windows. As explained in section 2, the back-projected contours are very elongated in the source-array direction. Our analysis provides accurate source location only in the perpendicular direction, which is sub-parallel to the EPGF strike. We hence extract the maximum of the MUSIC pseudo-spectrum along lines parallel to the source-array direction, then project these maxima onto the EPGF trace. Note that this aftershock has a slightly different strike (N290°) than the EPGF (N255°) but this difference is minor for this magnitude. The right column of Fig. 9 shows this quantity as a function of epicentral distance along the EPGF strike and of final time of the sliding window. Fig.9-d shows the aftershock is properly imaged as a compact source of 5 km size near its hypocenter, comparable to the typical rupture size of M6 earthquakes [*Wells and Coppersmith*, 1994]. This suggests little spatial smearing in our analysis at the 5 km scale and warrants imaging of the mainshock, which is possibly composed of multiple subevents.

Fig. 9c shows the results of our application of MUSIC to the VNSN recordings of the 2010 Haiti mainshock. We also applied two other popular array techniques, cubic-root stack and correlation stack with the same stations set and frequency band, shown in Figs. 9a and 9b respectively. Although all these array analysis techniques unambiguously indicate two prominent high-frequency subevents, our multitaper-MUSIC algorithm provides the images with the sharpest contrast between the subevents and the adjacent areas, as expected from our synthetic tests. Note that the peak locations of the MUSIC imaging are off the fault trace, to the South, due to limited resolution along the source-array direction at regional distance, which highlights the importance in regional array processing of a projection along the range direction onto the fault trace. The first subevent is located approximately 7 km east from the hypocenter. The second subevent is approximately 35 km further west (28km west from the hypocenter). This complexity is absent in the results of our analysis of the M6.1 aftershock (Fig.9-d) and hence is not due to path effects or other phases. The temporal evolution is better imaged by array processing at the peak frequency (0.4 Hz). In Fig.4-b, bilateral propagation is observed starting around t=10 s, when the last 10 s of the 30 s window contain the signal. The eastward front runs for about 10 km in about 3 s. The westward front shows a weaker MUSIC pseudo-spectra but its propagation can be consistently tracked over a distance of ~35 km and a duration of about 10 s (until t≈20 s). The rupture speed of both fronts is similar and consistent with usual sub-shear rupture speeds, given the shear wave speed of 3.65 km/s at 10 km depth in the Haiti region [*Bassin et al.*, 2000]. The observed features are compatible with the USArray source time functions and finite fault inversions described in the next section.

5. Comparison to independent observations

Our study is the first example of earthquake source imaging at regional distance with Pn waves for earthquakes of magnitude as low as 7. To build confidence in our results, we compare them here to other available observations. The complementarity between the different source analysis techniques provides an integrated view of the 2010 Haiti earthquake rupture process.

5.1. Source time functions at USArray and inferred rupture speed

The temporal separation between the two asperities is independently estimated from apparent source time functions obtained through deconvolution of teleseismic data by theoretical Green's functions (Fig.10) [*Chu et al.*, 2009]. We selected USArray stations with epicentral distances greater than 30 degrees to avoid complexities of the

P waveform due to triplication in the upper mantle. We computed synthetic Green's function using the generalized ray theory [*Helmberger*, 1983], the IASPEI91 1D global velocity model [*Kennett and Engdahl*, 1991] with the upper 30 km adjusted to a 4-layer Haiti regional crust model [*Bassin et al.*, 2000], and the CMT solution. The vertical component P waveforms and synthetic Green's functions are filtered from 0.01 to 1Hz and deconvolved in the time domain with the iterative technique of [*Kikuchi and Kanamori*, 1982] and with the non-negative least-squares algorithm. Both deconvolution techniques yield consistent results. To estimate the temporal separation between the subevents and its uncertainty, we considered 1000 stacks of randomly selected subsets containing 90% of the USArray stations. We measured the delay between the two prominent peaks in the stacked apparent source time functions. The resulting delays have a Gaussian distribution with mean t_1=5 s and standard deviation 0.02 s (Fig.10). We associate these to the two subevents found by our array analysis. The deconvolution analysis also indicates that the second subevent accounts for approximately one third of the total moment release, consistent with the multiple CMT solution of [*Nettles and Hjorleifsdottir*, 2010]. Their analysis also indicates that the second subevent has a thrust mechanism, in contrast to the near strike-slip mechanism of the first subevent. Nevertheless, at the azimuth of the USArray both mechanisms produce similar amplitudes and our choice to use the CMT solution to generate the Green's functions does not introduce a significant bias. The rupture speed can be reliably constrained by the apparent subevent delay of t_1=5 s and by the spatial subevent separation of 21 km between the two subevents centroids provided by our geodetic-only slip inversion (Figure S5, introduced in section 5.2). Considering a bilateral rupture, the real inter-subevent time delay is $t_0 = t_1 + \cos\theta (L_w - L_e)/c$, where θ is the angle between the fault strike and the source-array direction (40 degrees), c is the apparent P-wave speed (12 km/s at epicentral distance of 40 degrees), L_w and L_e are the distances of the centroid of the westward and eastward subevents, respectively (L_w = 21 km and L_e = 0 km). This yields a true inter-subevent time of 6.3 seconds. The implied rupture speed, 3.3 km/s, is within the usual sub-shear range. For reference the shear wave speed is 3.65 km/s at 10 km depth in the Haiti region [*Bassin et al.*, 2000]. Although our regional array back-projection analysis currently has large uncertainties on the rupture timing (see section 3.1), our back-projection result at the dominant frequency, 0.4 Hz (Fig. 4-b), is consistent with this sub-shear rupture speed.

5.2. Improved finite fault model

To evaluate how the results of the back-projection and USArray analysis of the source time function relate to other data sets and integrate in the global description of the rupture, we perform a joint source inversion based on teleseismic body waves and the various geodetic data available.

As detailed in previous studies [*Calais et al.*, 2010; *Hayes et al.*, 2010; *Hashimoto et al.*, 2011], the campaign GPS measurements and InSAR data provide a very good coverage of the Leogane delta where the rupture started and indicate that the deformation in this area is best explained by a fault segment dipping NNW. In agreement with those studies, we choose a fault strike of 254^0 and a dip angle of 55^0. This orientation of the fault plane is also compatible with the alignment of aftershocks along a $N75^0$ azimuth [*Mercier de Lépinay et al.*, 2011]. InSAR fringes (ALOS ascending track 137) and field measurements of the coastal vertical uplift in the area of the town of Petit Goave [*Hayes et al.*, 2010] suggest the earthquake also extended west and offshore of the Leogane delta. This hypothesis is supported by the aftershock catalog obtained from the Haiti-OBS local network of terrestrial and ocean-bottom seismic stations. In contrast with previous models, we do not cover this offshore area by simply extending the preferred Leogane fault geometry (i.e. dipping NNW) to the west, but refine the model with a distinct second fault segment dipping 45^0 to the NNE (strike N275^0). This NNW to NNE rotation in the fault strike is supported by the moment tensors of the aftershocks [*Nettles and Hjorleifsdottir*, 2010] and by the identification of bathymetric features with a similar orientation, such as the Trois Baies fault and the Transhaitian belt [*Mercier de Lépinay et al.*, 2011].

The location of the NEIC epicenter seems incompatible with our first fault segment as it would imply a very superficial rupture initiation (~2 km), and would not be compatible with the NEIC hypocentral depth (13 km). Moving the hypocenter in the northeast direction as suggested by the higher resolution Haiti-OBS aftershocks catalog (when compared to the NEIC catalog) brings the rupture initiation closer to the zone of high slip, as we would expect from the sharp onset of the rupture, and the hand-picked P wave onset (Fig. S1). The applied shift of a few kilometers is comparable to that applied by [*Mercier de Lépinay et al.*, 2011] in their finite fault inversion. To match this new epicenter location (72.54^0W, 18.46^0N) to our fault geometry, the hypocenter is fixed at a depth of 6 km.

The finite fault inversion is based on a Monte-Carlo type algorithm [*Ji et al.*, 2002] and uses teleseismic data (21 P waves and 13 SH waves bandpass filtered between 2 and 100 s), campaign GPS (data processing detailed in [*Calais et al.*, 2010]) and four InSAR images (data selection and processing detailed in [*Hayes et al.*, 2010]). We allow the rupture speed to vary from 3.0 to 3.6 km/s, that is +/-0.3 km/s around the rupture velocity inferred from the USArray analysis. We do not apply any minimization criteria on the seismic moment.

We obtain a slip model composed of two high slip patches, a first one centered on the epicenter and a second one with peak slip amplitude 21 km further west, starting 6 s after the onset of rupture (Fig.11). The data misfit in our updated model (Table S1) is comparable to previous studies [*Calais et al.*, 2010; *Hayes et al.*, 2010; *Hashimoto et al.*, 2011]. While the fit of the InSAR data is excellent (Fig. S2 and S3), the fit of the GPS data is of moderate quality (Fig.11): this is mainly due to the large misfit at station DFRT which, despite having one of the largest measured displacements (0.7 m measured in the center of the deformation area), cannot be adjusted either in azimuth or amplitude. At the location of station DFRT, ascending and descending InSAR tracks are too decorrelated to do a comparison of the 3D displacement. However, the smooth 3D pattern of deformation inferred from InSAR in the surrounding areas [Hayes et al., 2011] suggests that motion at DFRT is indeed affected by localized deformation. Calais et al. [2010] who also used InSAR and GPS data could not fit properly station DRFT. The vertical deformation along the coast was measured using coral data [Hayes et al., 2010]. Since most of those measurements are within the area where InSAR coverage allows to estimate the vertical motion (overlap of ascending and descending tracks) we did not include them in the inversion and only made sure that they are compatible *a posteriori*. This is true for all points (Fig. 11) except one subsidence measurement west of the surveyed area. This mismatch suggests that this point indeed represents a local effect, perhaps a local slump as described by [*McHugh et al.*, 2011] and [*Mercier de Lépinay et al.*, 2011] in the offshore survey of this area. Also, this subsidence very close from uplifted points reflects a change which is probably too localized to be properly reproduced by our simplified fault model.

Slip reaches a maximum of 10 meters (Fig. S4) at the center of the first patch (7 m for the second patch) which concentrates ⅔ of the total moment (3 10^{+19} N.m for the first patch, 1.5 10^{+19} N.m for the second). This result is similar to our analysis of the USArray data. In term of bulk parameters, we also find that the moment tensor of our solution (Fig. 11) and its seismic moment (4.5 10^{+19} N.m) are similar to the GCMT analysis [*Nettles and Hjorleifsdottir*, 2010]. The teleseismic data bound the duration of the source time function to less than 15 s and indicate that the first patch of slip was more impulsive than the second and smaller slip episode. The oblique rake along the rupture is consistent with the transcompressional regime in this region [Mercier de Lepinay et al., 2011] but doesn't support the hypothesis of a fully partitioned fault system where the EPGF would absorb all the strike-slip component [*Dixon et al.*, 1998; *Calais et al.*, 2002]

6. Discussion

6.1. Spatial complementarity between high and low frequency source properties

The primary results from the array analysis, the finite fault inversion and the source time function analysis suggest that the rupture propagates mostly westward breaking two main slip patches. In the low frequency view from finite fault inversion the first asperity is located near the epicenter and the second one is 21 km west and contributes to one third of the total seismic moment. On the other hand, the high frequency radiations suggest a distance of 35 km between the two asperities.

Since the back-projection provides subevents locations relative to the hypocenter, the choice of epicenter is essential in interpreting the result of the array processing. Assuming the epicenter given by NEIC, the subevent locations are consistent with the spatial pattern of the aftershocks (NEIC catalog), which cluster into two groups. The eastern group is close to the mainshock epicenter and the second group is located 30 to 40 km west. If we assume the NEIC hypocenter, the western subevent is well beyond the high slip patches derived from the finite fault model, implying possible slip further west offshore, unconstrained by geodesy. However, if we account for the NEIC catalog bias inferred from the Haiti-OBS aftershock catalog in Fig. 11 [*Mercier de Lépinay et al.*, 2011], the two subevents coincide with the terminal edges of the large slip areas. This difference is similar to the spatial complementarity between high and low frequency source properties inferred for several other earthquakes, including the 1989 Loma Prieta earthquake, the 1993 Kushiro-Oki earthquake [*Nakahara*, 2008] and the 2011 Tohoku-Oki earthquake [*Ide et al.*, 2011; *Meng et al.*, 2011; *Simons et al.*, 2011]. This complementarity can be interpreted as high frequency radiation generated by the stopping phases, associated with abrupt rupture speed reduction at the edge of the slip area. This mechanism of high-frequency radiation was first described in circular crack models [*Madariaga*, 1977; 1983] and was explained for general rupture front geometries through isochrone theory [*Bernard and Madariaga*, 1984; *Spudich and Frazer*, 1984]. This interpretation is also consistent with the aftershock locations clustering at the regions of stress concentration at the edges of the coseismic rupture. Note that the high frequency radiation is absent at the western end of the first asperity, implying a smoother stopping or rupture transition without stopping between the two asperities.

6.2. Extent of the offshore rupture

One aspect of the 2010 Haiti earthquake which still remains to be elucidated is the extent to which the rupture propagated offshore in areas that are not resolved by geodetic data. While there is no direct offshore geodetic measurements, InSAR and GPS data cannot be properly explained by on-land faulting alone. GPS station LEOG strongly points offshore and west of the Leogane delta (Fig. 11) despite the existence of an asperity east of that point (this asperity is directly visible in the descending InSAR track 447). The dense InSAR fringes of acending track 137 (Fig. S3) surround the coastline pointing to deformation in the center of the bay. All slip models based on either InSAR or GPS data found at least partial offshore faulting [*Calais et al.*, 2010; *Hayes et al.*, 2010; *Hashimoto et al.*, 2011; *Mercier de Lépinay et al.*, 2011], but the western extent of off-shore slip is not constrained by these data. Recent observations in the offshore region are suggestive of rupture extending further west than in our kinematic source model. Marine seismic reflection profiles indicate the existence of a large scale active anticline associated with the Trois Baies fault and the Transhaitian belt [*Mercier de Lépinay et al.*, 2011]. The aftershock locations derived from the Haiti-OBS campaign are offset by about 20 km NE relative to the NEIC catalog locations [*Mercier de Lépinay et al.*, 2011], implying that the western aftershock cluster is not onland but offshore. The Haiti-OBS catalog also confirms the existence of a cluster of aftershocks more than 30 km west of the epicenter, 10-20 km beyond the western end of coseismc slip in current source models.

In our kinematic source inversion based on teleseismic and geodetic data, slip is allowed to spread over more than 45 km west of the hypocenter (= maximum source duration × maximum rupture speed = 15 × 3 km). However, in the resulting model the slip remains confined to less than 22 km west of the epicenter. We obtained a similar slip distribution in a finite fault inversion based only on the static data sets, InSAR and GPS (Fig. S5 and S6) without constrain on the seismic moment, with comparable fit to the data (Fig. S7 and S8) and with a seismic moment (5.0 10^{+19} N.m) very close to the GCMT solution (4.7 10^{+19} N.m). Moreover, the InSAR fringes along the coast (tracks A138a and A447d in Fig. S8) tend to rotate slightly perpendicular to western end of our slip model, which suggests that there are no regions with larger slip further west.

In summary, several arguments indicate that the geodetic data did not miss any significant offshore deformation to the west. The spatial resolution of our regional back-projection is too coarse in the source-to-array direction (NNW-SSE) to provide an independent constrain on the distance between the coast and the second high-frequency source. However, the position of this second source along the cross-range direction (sub-parallel to the EPGF strike) is well constrained and is shown here to be consistent with the western end of offshore slip inferred from static deformation. This supports the idea that back-projection source imaging can identify the end tips of a rupture.

6.3. Advantage of regional array back-projection for earthquake source studies

Our study of the 2010 Haiti earthquake demonstrates that back-projection of P-waves recorded at regional distances can reveal the location of high frequency source radiation that are not resolvable by finite source inversions at teleseismic distance, which are now common practice. This new capability, improved by our analysis procedure combining multitaper and MUSIC techniques, allows to study the rupture of earthquakes with magnitude as low as 7 providing reliable spatial constraints. The approach requires that the approximate strike of the fault is known, but this information can usually be reliably extracted from the focal mechanism of the event. This implies that regional back-projection will be critical in the study of earthquakes when geodetic coverage is incomplete or local seismic networks are lacking, for instance in subduction zones. Moreover, the procedure can be automated for rapid, possibly real-time, earthquake analysis, combing the fault strike information from fast moment tensor inversions. In that sense, the VNSN alone has a great potential for the analysis of earthquake hazard for the whole Caribbean-North America plate boundary. The high frequency aspects of the source process derived from array back-projection are particularly useful to estimate potential damage in regions where the vulnerable components of the building stock are dominated by low rise (short period) buildings. In a more global perspective, the statistical analysis of the last 120 years of earthquakes demonstrate that most of the devastating earthquakes occur in continental interiors on previously unmapped faults [*England and Jackson*, 2011]. Thus, with the ongoing development of regional seismic networks, many of those devastating earthquakes will still happen at regional distance from networks, and require the resolving power of regional back-projection.

7. Conclusions

In this study, we developed a back-projection source imaging technique for body waves recorded by seismic arrays at regional distances (Pn waves). The technique combines the Multiple Source Classification (MUSIC) method with multi-taper cross-spectral estimation to achieve sharper source imaging than existing methods. This technique allowed us to extract key aspects of the rupture process of the 2010 Haiti earthquake from recordings by the Venezuela National Seismic Network (VNSN). In particular, it provides the locations of high frequency source radiation. When integrated with independent studies based on teleseismic and geodetic data of this earthquake, our results indicate bilateral rupture at subshear speed, with a much longer rupture segment towards the West. Prominent high frequency radiation originates from rupture arrest phases at the tip of the main slip areas. Additional rupture offshore is not supported by our analysis. Our results demonstrate how regional array studies can contribute to the characterization of seismic sources in the Caribbean region and elsewhere, particularly in offshore regions where local seismic network or geodetic data coverage are not available, with potential application for rapid earthquake response.

Figure captions

Fig. 1 Haiti earthquake recorded by the Venezuela National Seismic Network. The triangles denote the 22 broadband stations of the VNSN that recorded the 2010 Haiti earthquake. The 13 stations shown in green were selected for our analysis based on their mutual coherency. The red star indicates the epicenter (NEIC) of the Haiti event. The inset shows vertical component seismograms filtered from 0.2 to 0.7 Hz, aligned on their first P arrival and normalized by the standard deviation of their first 10 seconds.

Fig. 2 Array response patterns, of the VNSN (left) and USArray (right) back-projected into the Haiti source region. plotted in map view. The color scale indicates the power of the array response, normalized by its peak value. The yellow line denotes the trace of the EPGF [*Calais et al.,* 2010]. The white dot is the location of the NEIC epicenter.

Fig. 3 Station selection based on array data correlation matrix made of the correlation coefficients between all pairs of stations (indicated by the color scale). The stations are reordered by a clustering algorithm. The black box encompasses the most mutually coherent subset of stations, which is used in our array analysis.

Fig. 4 Dependence of MUSIC results on the assumed size N of the signal subspace, at 0.4 Hz with N=1 to 4 (a to d, respectively). The MUSIC pseudo-spectrum as a function of along-strike position with respect to the hypocenter is shown in color and normalized by its maximum in each time window. The time axis is defined as the final time of the sliding windows of 30 s long sliding windows. The horizontal axis is the distance along the fault with respect to the epicenter. The yellow dashed lines and the black dots in figure b (N=2) show the bilateral rupture trend and subevent locations.

Fig. 5 Comparison of resolution between array processing techniques. Two plane waves, A and B, impinge on a linear array. The azimuth of A is fixed at 0 degrees while the azimuth of B is varied from -10 to 0 degrees. Four array processing techniques are considered: classical beamforming (a), cubic root stacking (b), correlation stacking (c) and MUSIC (d). Each curve in the top plots shows the stack (a-c) or pseudo-spectra (d) as a function of relative azimuth with respect to A for a given azimuth separation between A and B (value indicated in the legend). The bottom panels show the same quantities in color plots. The white dots mark the half-width of the two largest maxima at a given azimuth of B. Correlation stacking provides better resolution than beamforming and cubic root stacking. However, MUSIC can resolve waves with azimuth separation as small as 3 degrees, achieving at least twice higher resolution (minimum resolvable azimuthal separation) than the other methods.

Fig. 6 Synthetic test of array processing for the Haiti earthquake scenario. The earthquake is modeled by two point sources, the first one at the hypocenter and the second one at a distance *d* westward along the fault trace. We applied cubic root stacking (a), correlation stacking (b) and MUSIC (c). The left two columns are map view back-projection images for d = 30 km (10s delay), in the time windows that start at the beginning of the first (t = 0 s) and second (t = 10 s) source. The green asterisk and red circle indicate the locations of the first and second source. The right two columns show the projection of the images onto the fault trace, parallel to the source-array direction, as a function of the distance *d*. The white lines indicate the locations of the two sources. We considered moment ratios between first and second sources of 1:1 and 2:1. In the case of 2:1 source ratio, The cubic root stacking and correlation stacking methods show resolution limit of about 35km, while the resolution limit of MUSIC is about 25 km and the location error is approximately 5 km for each subevent.

Fig. 7 Synthetic and aftershock seismograms at the VNSN. The top figure (a) shows the vertical component of the synthetic seismograms of the mainshock filtered from 0.2 to 0.7 Hz, assuming a point source with mechanism given by the CMT solution. The bottom figure (b) shows the vertical recordings of a M5.9 aftershock recorded at the VNSN with the same filtering applied.

Fig. 8 Interference issues associated with the beamforming analysis. Results of two synthetic tests with a composite source comprising two subevents 15 km (top) and 30 km (bottom) apart with Green's function computed with the Frequency-Wavenumber method of [*Zhu and Rivera*, 2002]. Left: maps of beam amplitude back-projected into the source region. Right: synthetic seismograms. The stations deficient in low frequencies, due to interference effects, are colored in red.

Fig. 9 Array analysis of the Haiti event. Considering cubic root stacking (a), correlation stacking (b) and MUSIC (c). The left two columns shows back-projection images from 30s-long time windows ending at t=10 s and 30 s, respectively (t=0 s is the arrival time). The yellow curve indicates the trace of the EPGF [*Calais et al.*, 2010]. The green line in the top-left plot is the major axis of the array response pattern along which we project the array analysis onto the fault. The MUSIC analysis has higher resolution and can clearly separate two asperities. The right column shows the projection on the fault as a function of final time of the sliding window. The MUSIC analysis of the largest aftershock (M5.9) is shown in panel (d).

Fig. 10 Source time function from USArray data. The triangles in the map show the USArray stations that recorded the Haiti event. The triangles in blue are all USArray stations that record the Haiti event. The stations in green have epicentral distance greater than 30 degree and good signal to noise ratio, and were selected for deconvolution. The red star is the epicenter of the Haiti earthquake. The red triangle is station R23A. The inset shows (a) the recorded and synthetic seismograms, (b) the source time function retrieved by non-negative least square (red) and Kikuchi-Kanamori deconvolution techniques (green) at station R23A; and (c) source time functions (green) from all selected USArray stations and the stacked source time function (red). (d) histogram showing the delay between the two peaks from bootstrapping the stacked source time functions and the best-fit Gaussian distribution (red curve).

Fig.11. Improved joint finite fault inversion of the Haiti event. Surface projection of the slip distribution inferred from the joint inversion of teleseismic, GPS and InSAR data. The black and red arrows represent the recorded and model predicted campaign GPS vectors respectively. The two orange dash lines mark the locations of the subevents identified by MUSIC back-projection assuming our refined mainshock epicenter as reference (red star). The black empty star is the USGS epicenter. The small empty circles are the aftershock epicenters of the Haiti-OBS campaign. The three inset maps show the location of the study area (top left), the measured and predicted coastal uplift (top right) and the inverted source time function (lower right).

On the source time function plot, the blue and green curve show the contribution of the Leogane and offshore fault segments respectively.

Reference

Bassin, C., G. Laske, and G. Masters (2000), The Current Limits of Resolution for Surface Wave Tomography in North America, *EOS Trans AGU, 81, F897, 2000.*, *81*(F897).

Bernard, P., and R. Madariaga (1984), High-Frequency Seismic Radiation from a Buried Circular Fault, *Geophys J Roy Astr S*, *78*(1), 1-17.

Borcea, L., G. Papanicolaou, and C. Tsogka (2005), Interferometric array imaging in clutter, *Inverse Probl*, *21*(4), 1419-1460, doi: 10.1088/0266-5611/21/4/015.

Calais, E., Y. Mazabraud, B. M. de Lepinay, P. Mann, G. Mattioli, and P. Jansma (2002), Strain partitioning and fault slip rates in the northeastern Caribbean from GPS measurements, *Geophys Res Lett*, *29*(18), doi: 10.1029/2002gl015397.

Calais, E., A. Freed, G. Mattioli, F. Amelung, S. Jonsson, P. Jansma, S. H. Hong, T. Dixon, C. Prepetit, and R. Momplaisir (2010), Transpressional rupture of an unmapped fault during the 2010 Haiti earthquake, *Nat Geosci*, *3*(11), 794-799, doi: 10.1038/Ngeo992.

Chu, R., L. P. Zhu, and D. V. Helmberger (2009), Determination of earthquake focal depths and source time functions in central Asia using teleseismic P waveforms, *Geophys Res Lett*, *36*, doi: 10.1029/2009gl039494.

Dixon, T. H., F. Farina, C. DeMets, P. Jansma, P. Mann, and E. Calais (1998), Relative motion between the Caribbean and North American plates and related boundary zone deformation from a decade of GPS observations, *J Geophys Res-Sol Ea*, *103*(B7), 15157-15182.

England, P., and J. Jackson (2011), Uncharted seismic risk, *Nat Geosci*(4), 348-349.

Fletcher, J. B., P. Spudich, and L. M. Baker (2006), Rupture propagation of the 2004 Parkfield, California, earthquake from observations at the UPSAR, *B Seismol Soc Am*, *96*(4), S129-S142, doi: 10.1785/0120050812.

Goldstein, P., and R. J. Archuleta (1991), Deterministic Frequency-Wave-Number Methods and Direct Measurements of Rupture Propagation during Earthquakes Using a Dense Array - Theory and Methods, *J Geophys Res-Solid*, *96*(B4), 6173-6185.

Guilbert, J., J. Vergoz, E. Schissele, A. Roueff, and Y. Cansi (2005), Use of hydroacoustic and seismic arrays to observe rupture propagation and source extent of the M-w=9.0 Sumatra earthquake, *Geophys Res Lett*, *32*(15), doi: 10.1029/2005gl022966.

Hashimoto, M., Y. Fukushima, and Y. Fukahata (2011), Fan-delta uplift and mountain subsidence during the Haiti 2010 earthquake, *Nat Geosci*, *4*(4), 255-259, doi: 10.1038/Ngeo1115.

Hayes, G. P., et al. (2010), Complex rupture during the 12 January 2010 Haiti earthquake, *Nat Geosci*, *3*(11), 800-805, doi: 10.1038/Ngeo977.

Helmberger, D. V. (1983), Theory and application of synthetic seismograms, in Earthquakes: Observation, Theory and Interpretation, *Soc. Ital. di Fis., Bolgna, Italy.*, 174– 222.

Ide, S., A. Baltay, and G. Beroza (2011), Shallow Dynamic Overshoot and Energetic Deep Rupture in the 2011 Mw 9.0 Tohoku-Oki Earthquake, *Sci China Ser C*, *332*(1426).

Ishii, M., P. M. Shearer, H. Houston, and J. E. Vidale (2005), Extent, duration and speed of the 2004 Sumatra-Andaman earthquake imaged by the Hi-Net array, *Nature*, *435*(7044), 933-936, doi: 10.1038/Nature03675.

Ji, C., D. J. Wald, and D. V. Helmberger (2002), Source description of the 1999 Hector Mine, California, earthquake, part I: Wavelet domain inversion theory and resolution analysis, *B Seismol Soc Am*, *92*(4), 1192-1207.

Kennett, B. L. N., and E. R. Engdahl (1991), Traveltimes for Global Earthquake Location and Phase Identification, *Geophys J Int*, *105*(2), 429-465.

Kikuchi, M., and H. Kanamori (1982), Inversion of Complex Body Waves, *B Seismol Soc Am*, *72*(2), 491-506.

Krim, H., and M. Viberg (1996), Two decades of array signal processing research - The parametric approach, *Ieee Signal Proc Mag*, *13*(4), 67-94.

Madariaga, R. (1977), High-Frequency Radiation from Crack (Stress Drop) Models of Earthquake Faulting, *Geophys J Roy Astr S*, *51*(3), 625-651.

Madariaga, R. (1983), High-Frequency Radiation from Dynamic Earthquake Fault Models, *Ann Geophys*, *1*(1), 17-23.

McHugh, C. M., et al. (2011), Offshore sedimentary effects of the 12 January 2010 Haiti earthquake, *Geology*, *39*(8), 723-726, doi: 10.1130/G31815.1.

Mendoza, C. (2005), Earthquake source-parameter estimation using regional waveforms: Implications for tsunami alerting in the Caribbean, *Geophys Res Lett*, *32*(24), -, doi: 10.1029/2005gl024435.

Meng, L. S., A. Inbal, and J. P. Ampuero (2011), A window into the complexity of the dynamic rupture of the 2011 Mw 9 Tohoku-Oki earthquake, *Geophys Res Lett*, *38*, doi: 10.1029/2011gl048118.

Mercier de Lépinay et al., B. (2011), The 2010 Haiti earthquake: A complex fault pattern constrained by seismologic and tectonic observations, *Geophysical Research Letters*

38, doi: 10.1029/2011GL049799.

Nakahara, H. (2008), Seismogram Envelope Inversion for High-Frequency Seismic Energy Radiation from Moderate-to-Large Earthquakes, *Adv Geophys*, *50*, 401-426, doi: 10.1016/S0065-2687(08)00015-0.

Nettles, M., and V. Hjorleifsdottir (2010), Earthquake source parameters for the 2010 January Haiti main shock and aftershock sequence, *Geophys J Int*, *183*(1), 375-380, doi: 10.1111/j.1365-246X.2010.04732.x.

Prentice, C. S., P. Mann, A. J. Crone, R. D. Gold, K. W. Hudnut, R. W. Briggs, R. D. Koehler, and P. Jean (2010), Seismic hazard of the Enriquillo-Plantain Garden fault in Haiti inferred from palaeoseismology, *Nat Geosci*, *3*(11), 789-793, doi: 10.1038/Ngeo991.

Rost, S., and C. Thomas (2002), Array seismology: Methods and applications, *Rev Geophys*, *40*(3), doi: 10.1029/2000rg000100.

Schmidt, R. O. (1986), Multiple Emitter Location and Signal Parameter-Estimation, *Ieee T Antenn Propag*, *34*(3), 276-280.

Simons, M., et al. (2011), The 2011 Magnitude 9.0 Tohoku-Oki Earthquake: Mosaicking the Megathrust from Seconds to Centuries, *Science*, *332*(6036), 1421-1425, doi: 10.1126/science.1206731.

Spudich, P., and E. Cranswick (1984), Direct Observation of Rupture Propagation during the 1979 Imperial Valley Earthquake Using a Short Baseline Accelerometer Array, *B Seismol Soc Am*, *74*(6), 2083-2114.

Spudich, P., and L. N. Frazer (1984), Use of Ray Theory to Calculate High-Frequency Radiation from Earthquake Sources Having Spatially-Variable Rupture Velocity and Stress Drop, *B Seismol Soc Am*, *74*(6), 2061-2082.

Thomson, D. J. (1982), Spectrum Estimation and Harmonic-Analysis, *P Ieee*, *70*(9), 1055-1096.

Tromp, J., D. Komatitsch, and Q. Y. Liu (2008), Spectral-element and adjoint methods in seismology, *Commun Comput Phys*, *3*(1), 1-32.

Vallee, M., M. Landes, N. M. Shapiro, and Y. Klinger (2008), The 14 November 2001 Kokoxili (Tibet) earthquake: High-frequency seismic radiation originating from the transitions between sub-Rayleigh and supershear rupture velocity regimes, *J Geophys Res-Sol Ea*, *113*(B7), doi: 10.1029/2007jb005520.

Vandecar, J. C., and R. S. Crosson (1990), Determination of Teleseismic Relative Phase Arrival Times Using Multi-Channel Cross-Correlation and Least-Squares, *B Seismol Soc Am*, *80*(1), 150-169.

Wei, S., Z. Zhan, Y. Luo, S. Ni, Y. Chen, and D. V. Helmberger (2009), Rapid Regional Centroid Solutions, *American Geophysical Union, Fall Meeting 2009, abstract #S13A-1734*

Wells, D. L., and K. J. Coppersmith (1994), New Empirical Relationships among Magnitude, Rupture Length, Rupture Width, Rupture Area, and Surface Displacement, *B Seismol Soc Am*, *84*(4), 974-1002.

Zhu, L. P., and D. V. Helmberger (1996), Advancement in source estimation techniques using broadband regional seismograms, *B Seismol Soc Am*, *86*(5), 1634-1641.

Zhu, L. P., and L. A. Rivera (2002), A note on the dynamic and static displacements from a point source in multilayered media, *Geophys J Int*, *148*(3), 619-627.

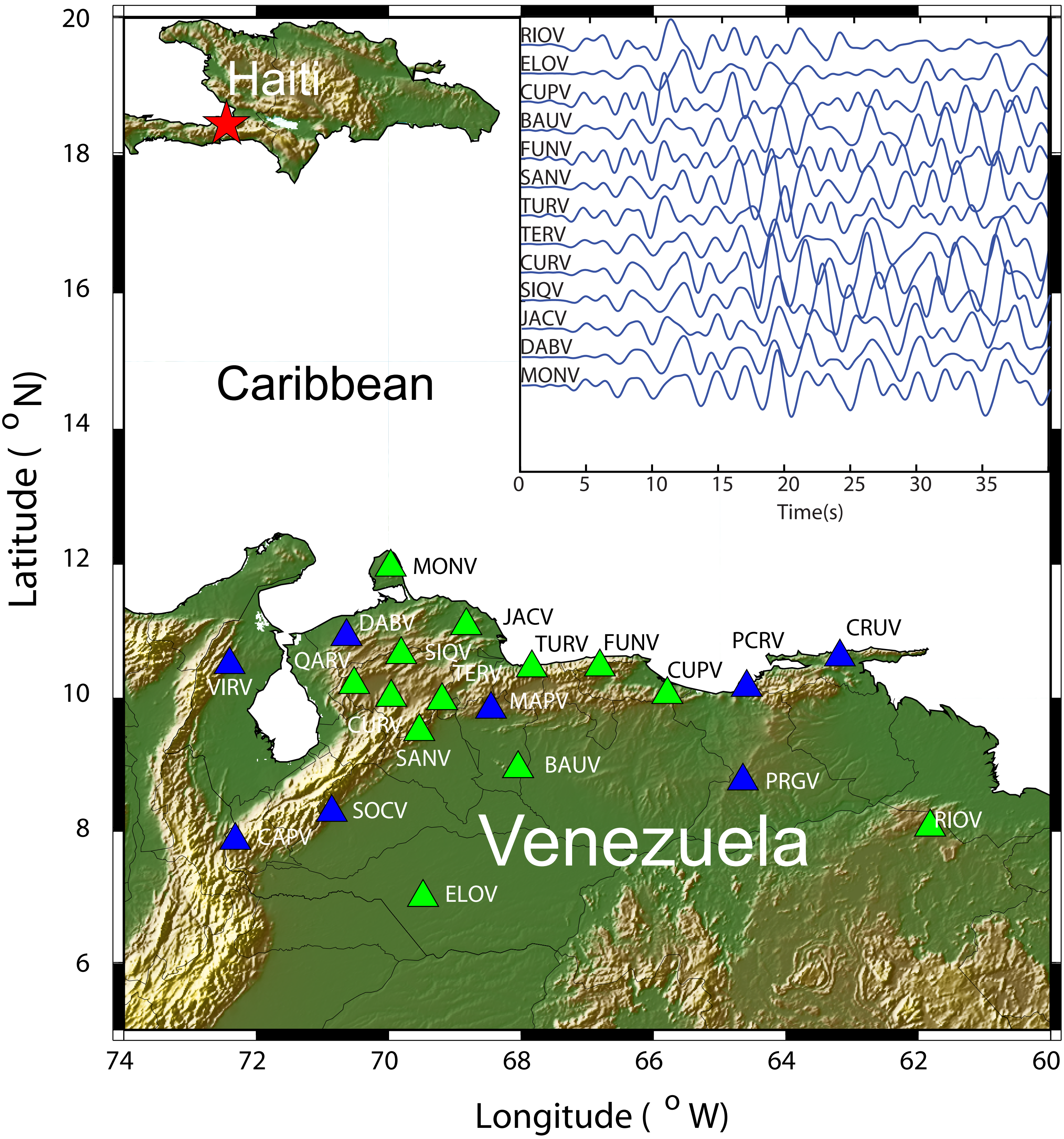

Haiti
Caribbean
Venezuela
RIOV
ELOV
CUPV
BAUV
FUNV
SANV
TURV
TERV
CURV
SIQV
JACV
DABV
MONV
Time(s)
MONV
DABV
JACV
QARV
SIQV
TERV
TURV
FUNV
PCRV
CRUV
CUPV
VIRV
MAPV
CURV
SANV
BAUV
PRGV
SOCV
CAPV
RIOV
ELOV
Latitude (o N)
Longitude (o W)

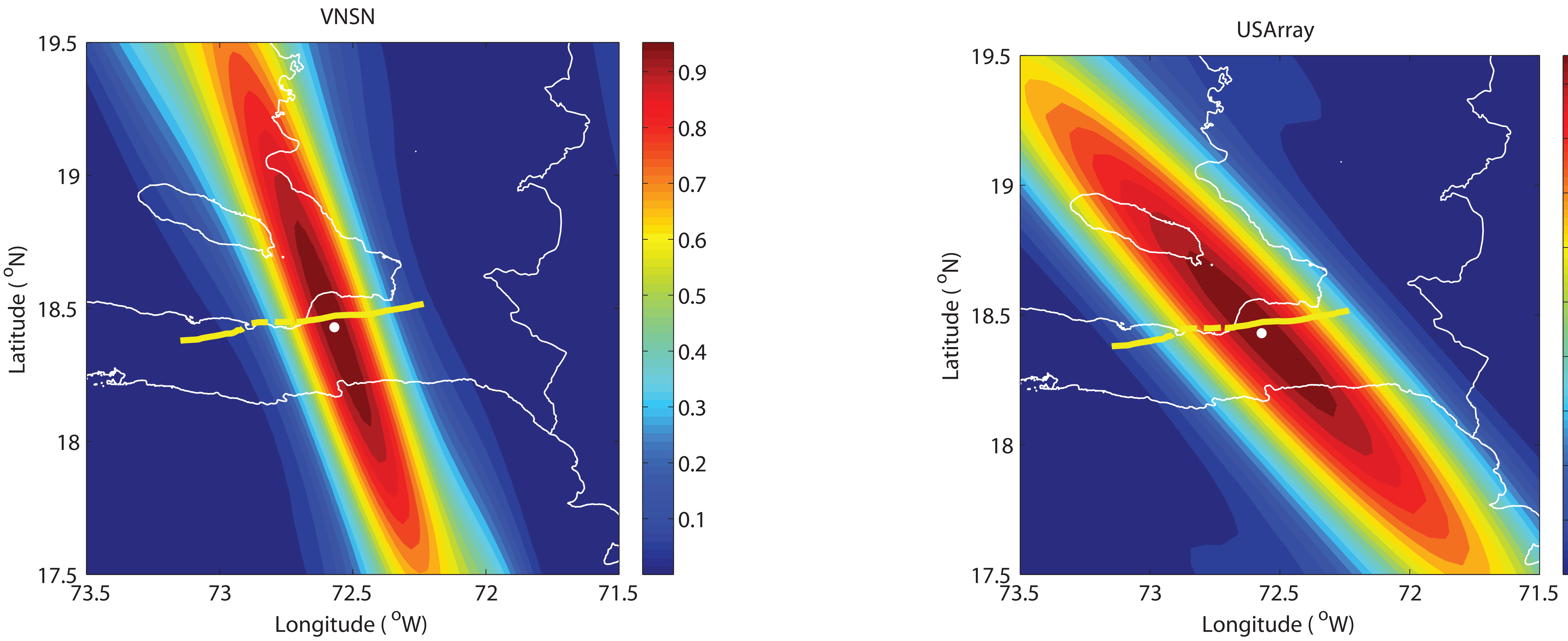

VNSN
USArray
Latitude (°N)
Longitude (°W)
19.5
19
18.5
18
17.5
73.5
73
72.5
72
71.5
0.9
0.8
0.7
0.6
0.5
0.4
0.3
0.2
0.1

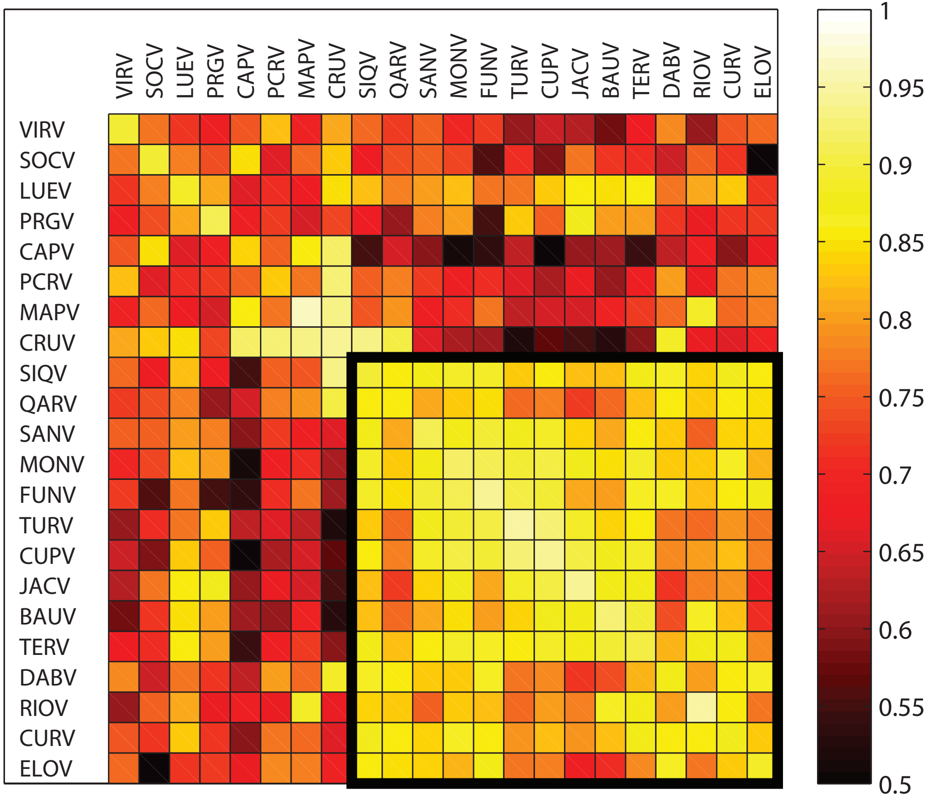
VIRV
SOCV
LUEV
PRGV
CAPV
PCRV
MAPV
CRUV
SIQV
QARV
SANV
MONV
FUNV
TURV
CUPV
JACV
BAUV
TERV
DABV
RIOV
CURV
ELOV
1
0.95
0.9
0.85
0.8
0.75
0.7
0.65
0.6
0.55
0.5

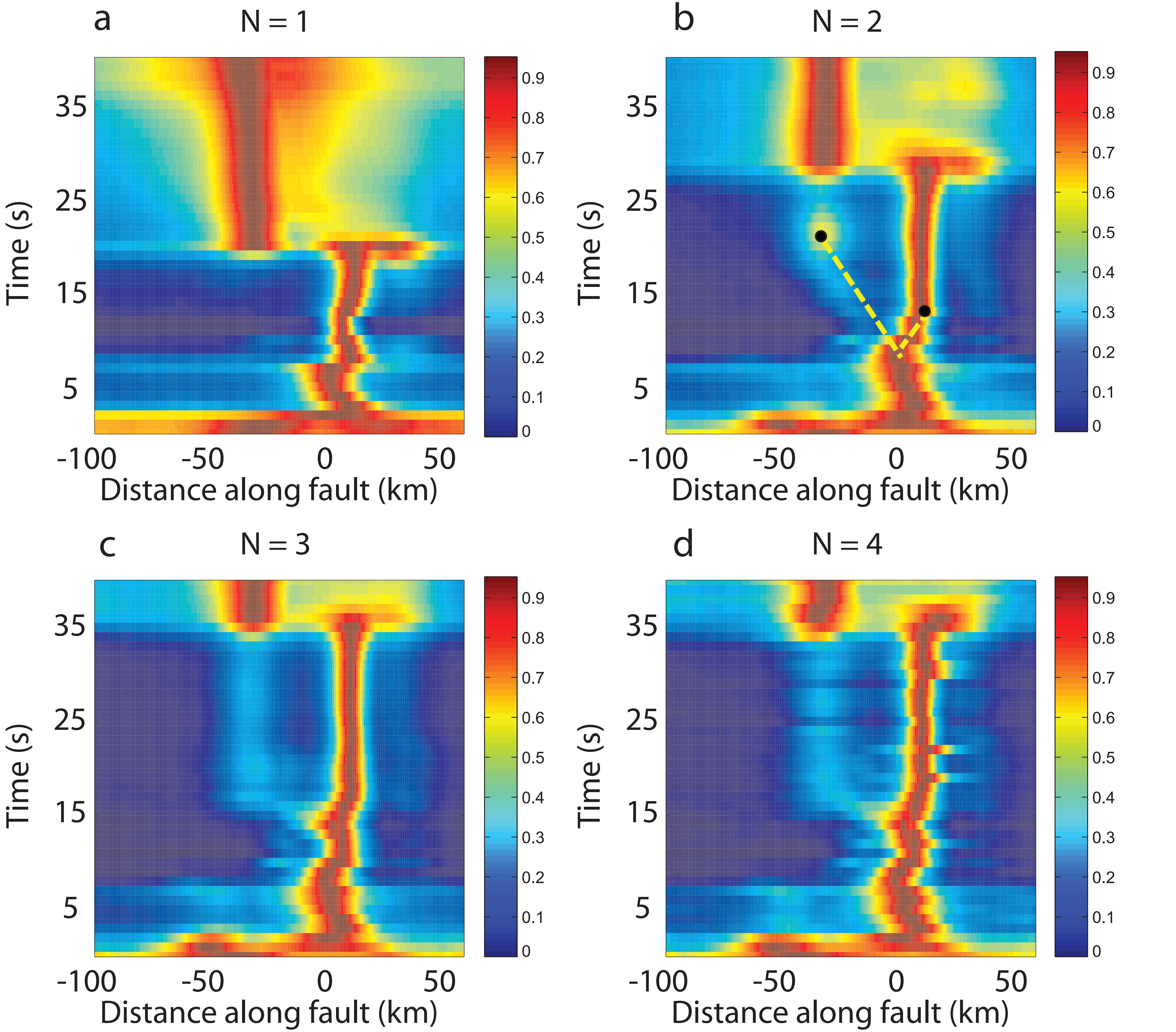

a
N = 1
b
N = 2
c
N = 3
d
N = 4
Time (s)
Distance along fault (km)
-100
-50
0
50
5
15
25
35
0
0.1
0.2
0.3
0.4
0.5
0.6
0.7
0.8
0.9

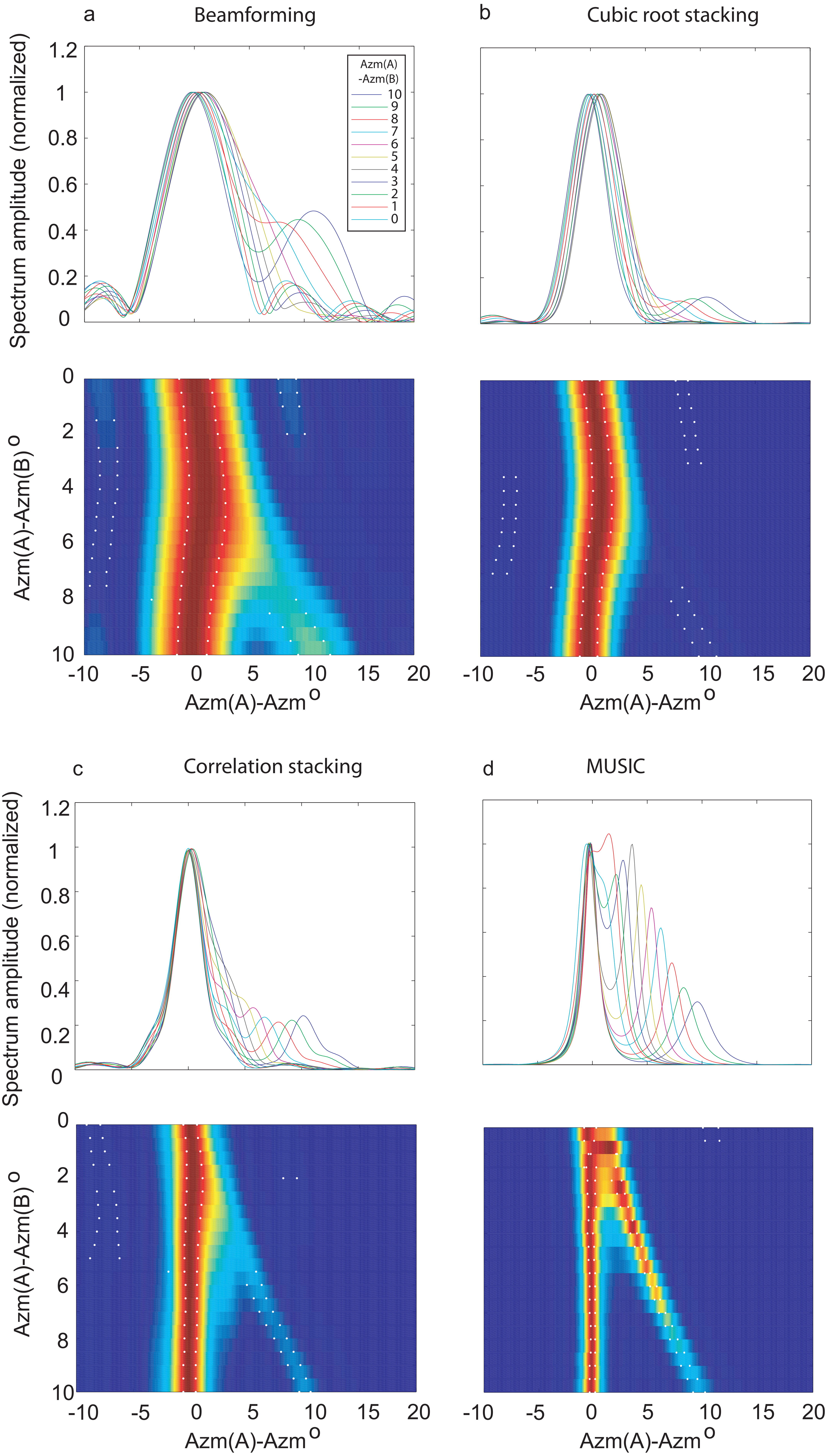
a
Beamforming
b
Cubic root stacking
c
Correlation stacking
d
MUSIC
Spectrum amplitude (normalized)
Azm(A)-Azm(B) o
Azm(A)-Azm o
Azm(A)
-Azm(B)
10
9
8
7
6
5
4
3
2
1
0

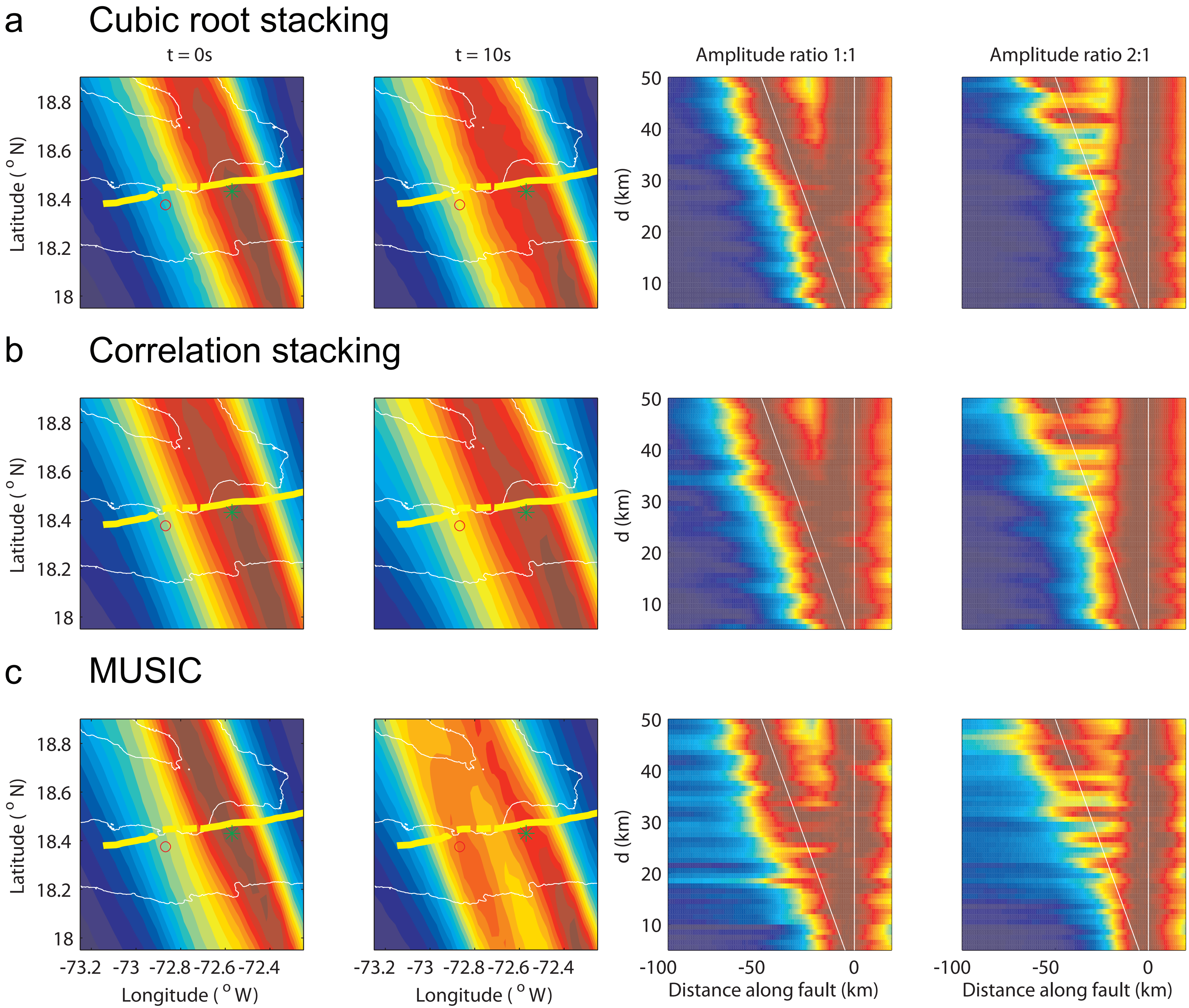

a
Cubic root stacking
t = 0s
t = 10s
Amplitude ratio 1:1
Amplitude ratio 2:1
b
Correlation stacking
c
MUSIC
Latitude (° N)
18.8
18.6
18.4
18.2
18
d (km)
50
40
30
20
10
-73.2 -73 -72.8 -72.6 -72.4
Longitude (° W)
-100 -50 0
Distance along fault (km)

a Synthetic seismogram

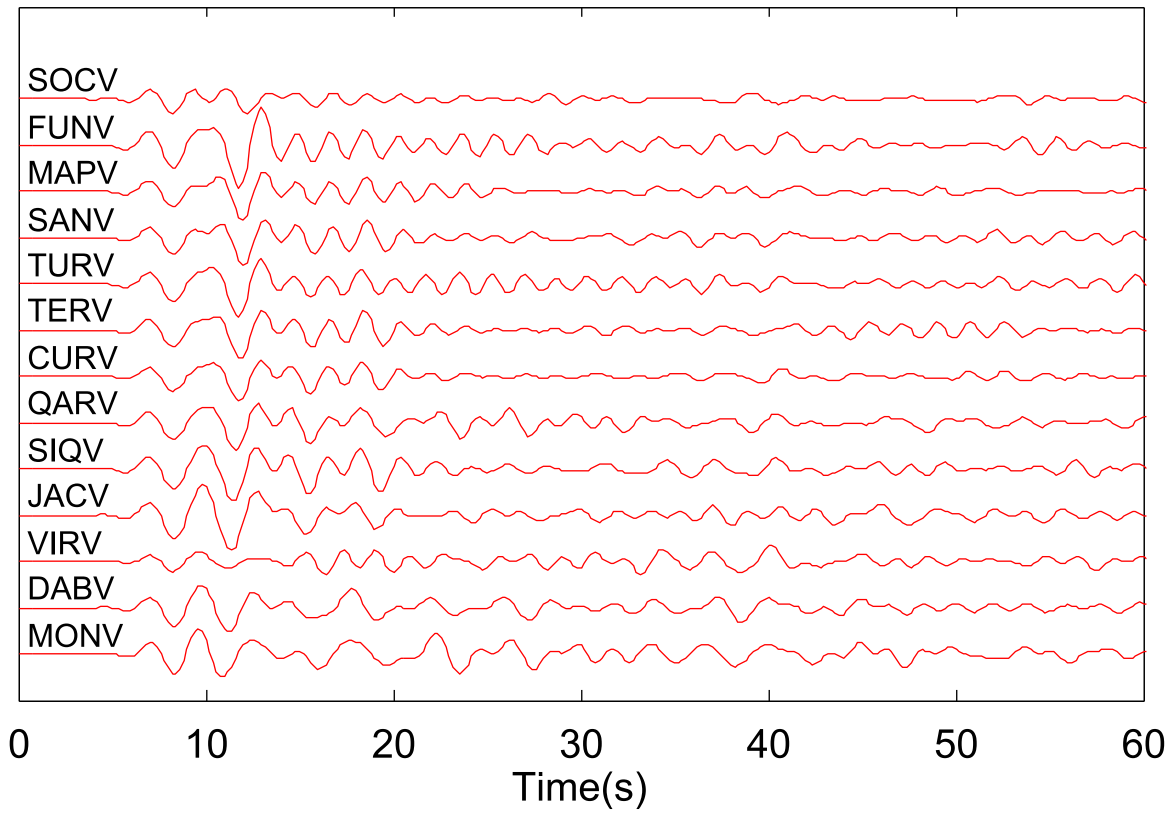

b Observed aftershock

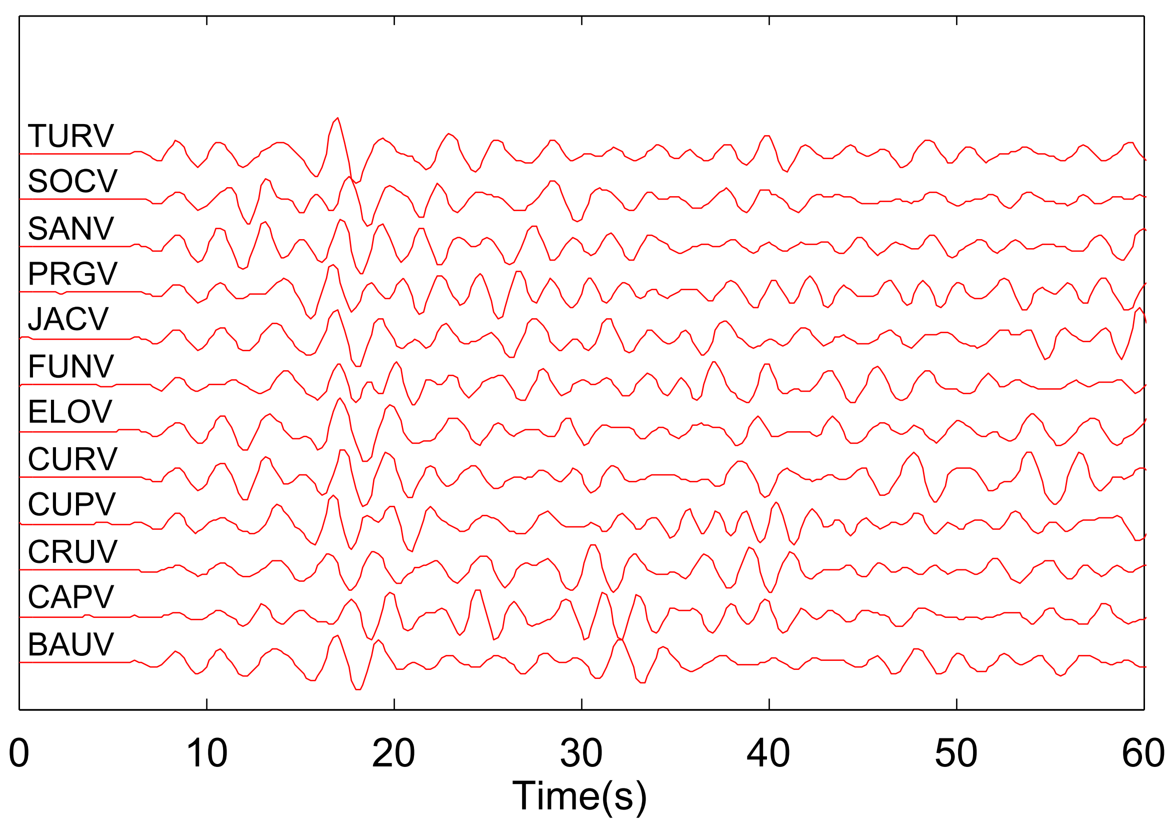

Two sources 15km apart

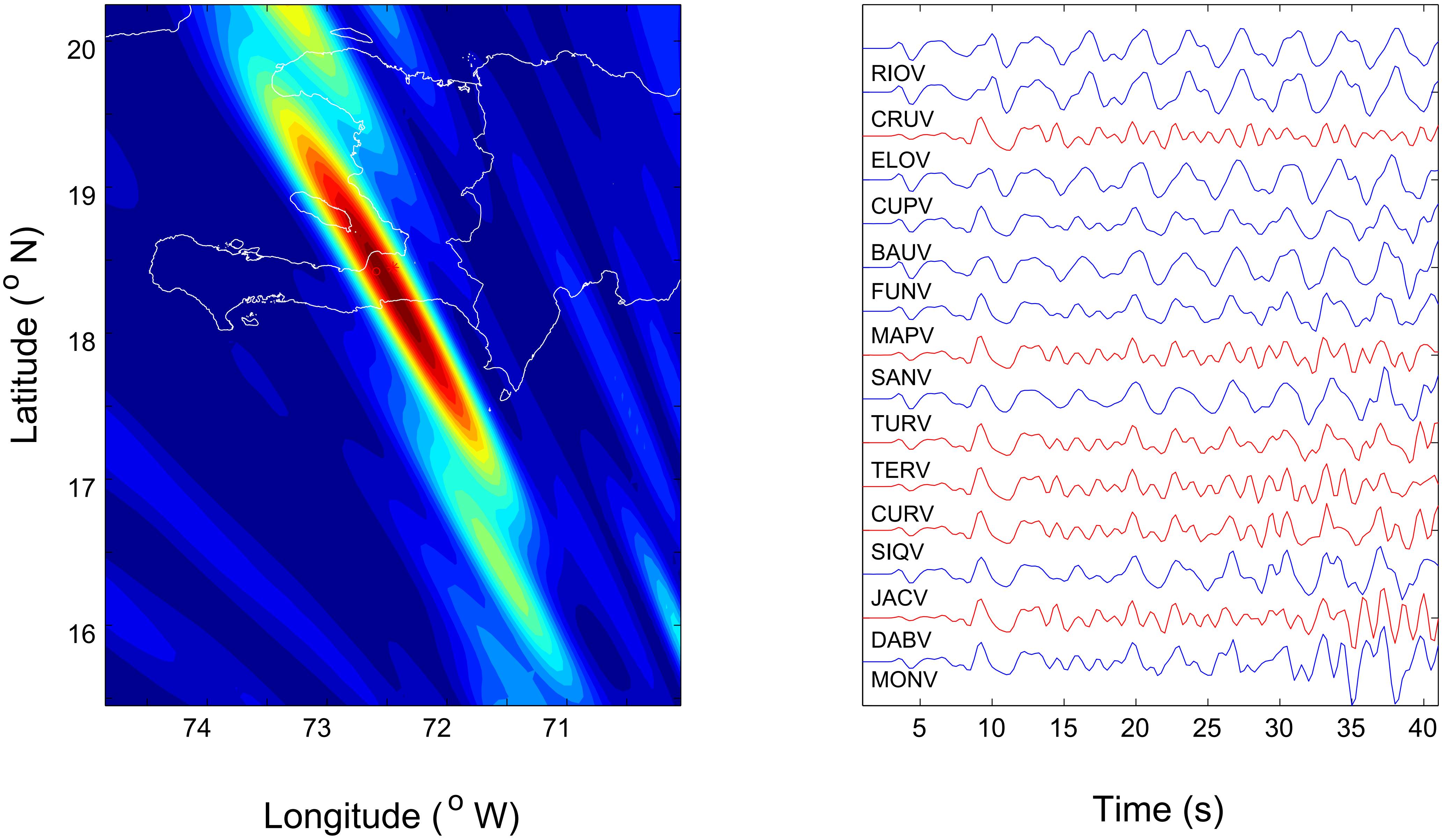

Two sources 30km apart

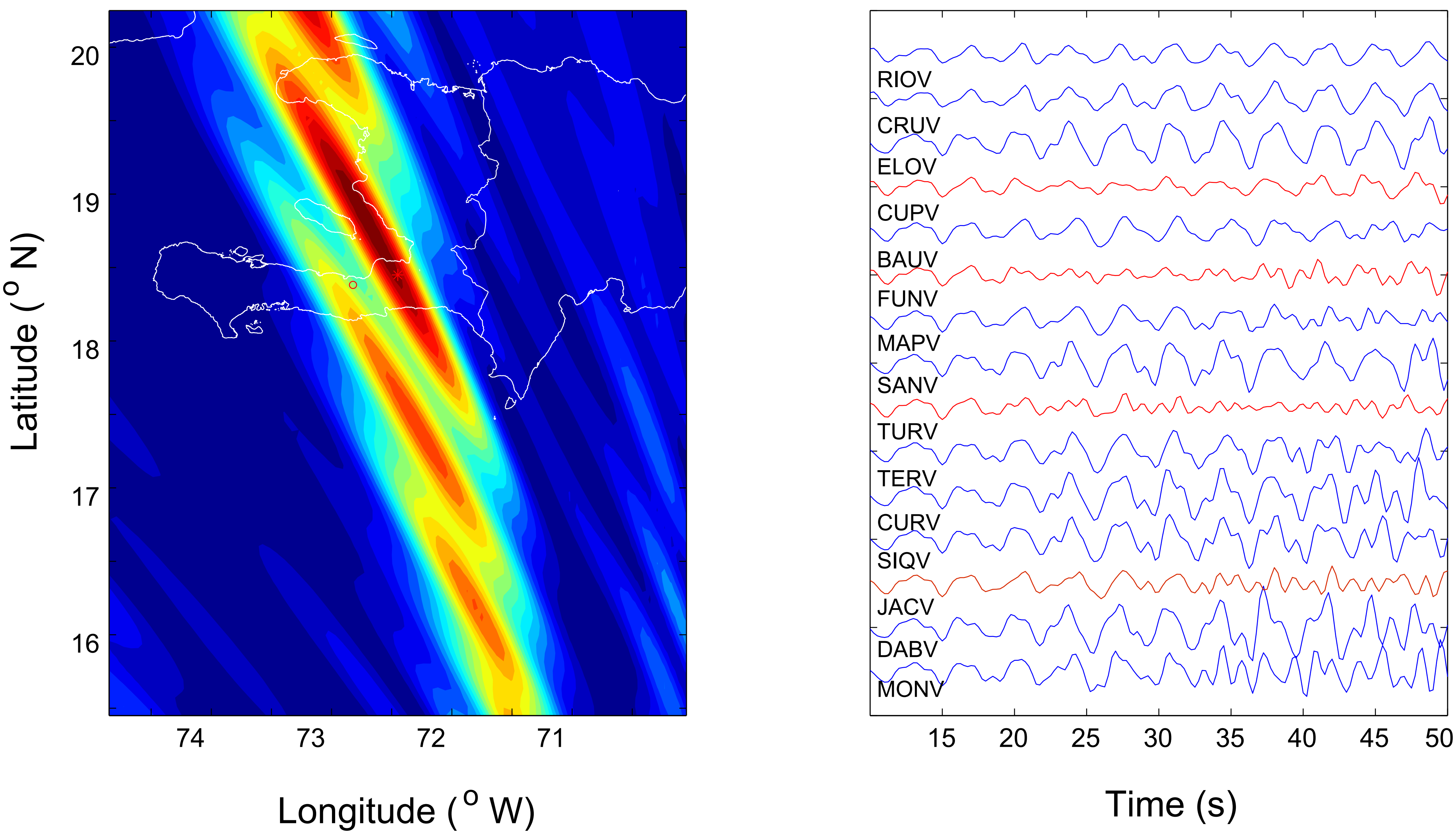

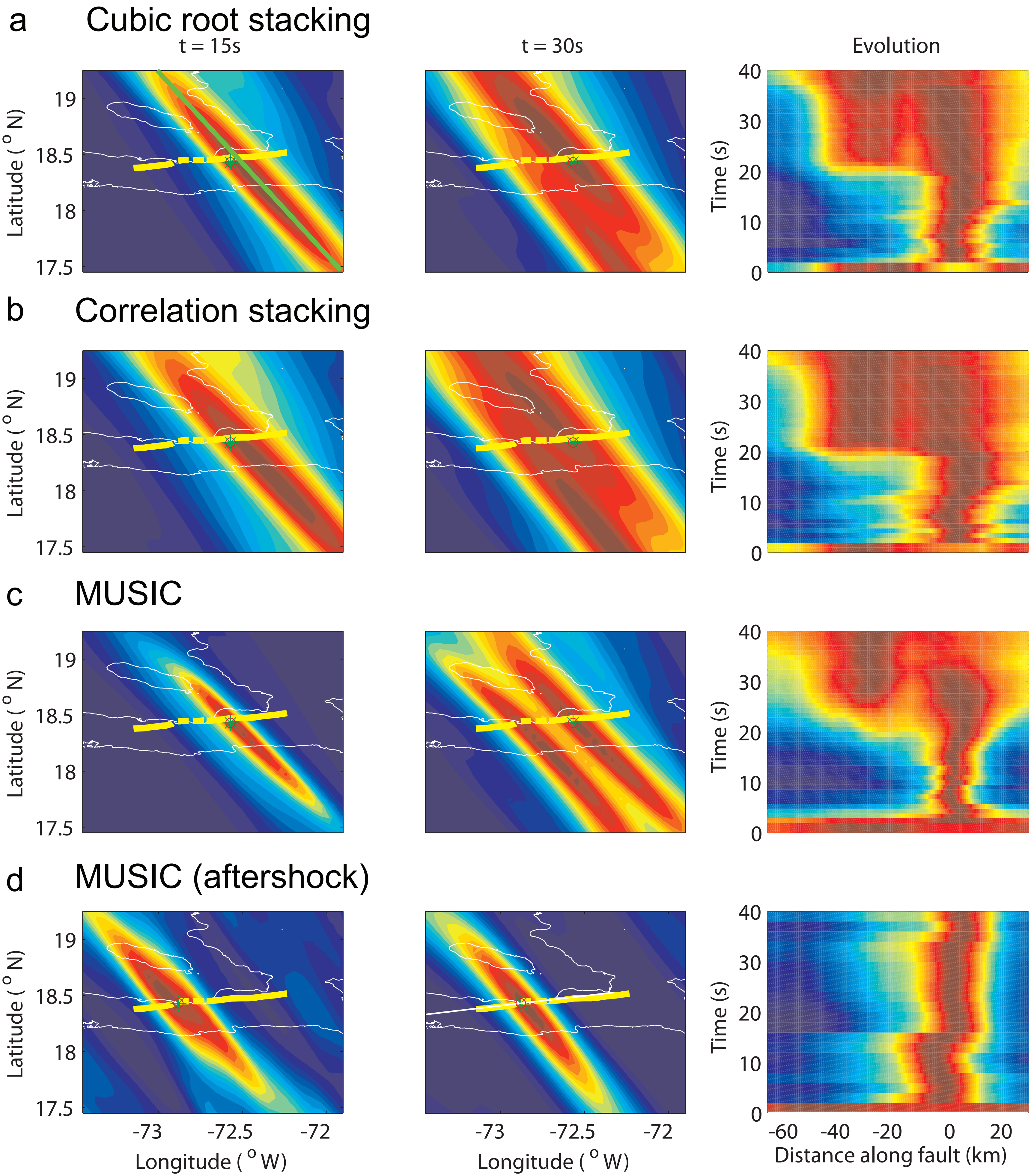
a
Cubic root stacking
t = 15s
t = 30s
Evolution
b
Correlation stacking
c
MUSIC
d
MUSIC (aftershock)
Latitude (^{o} N)
19
18.5
18
17.5
Time (s)
40
30
20
10
0
-73
-72.5
-72
Longitude (^{o} W)
-60
-40
-20
0
20
Distance along fault (km)

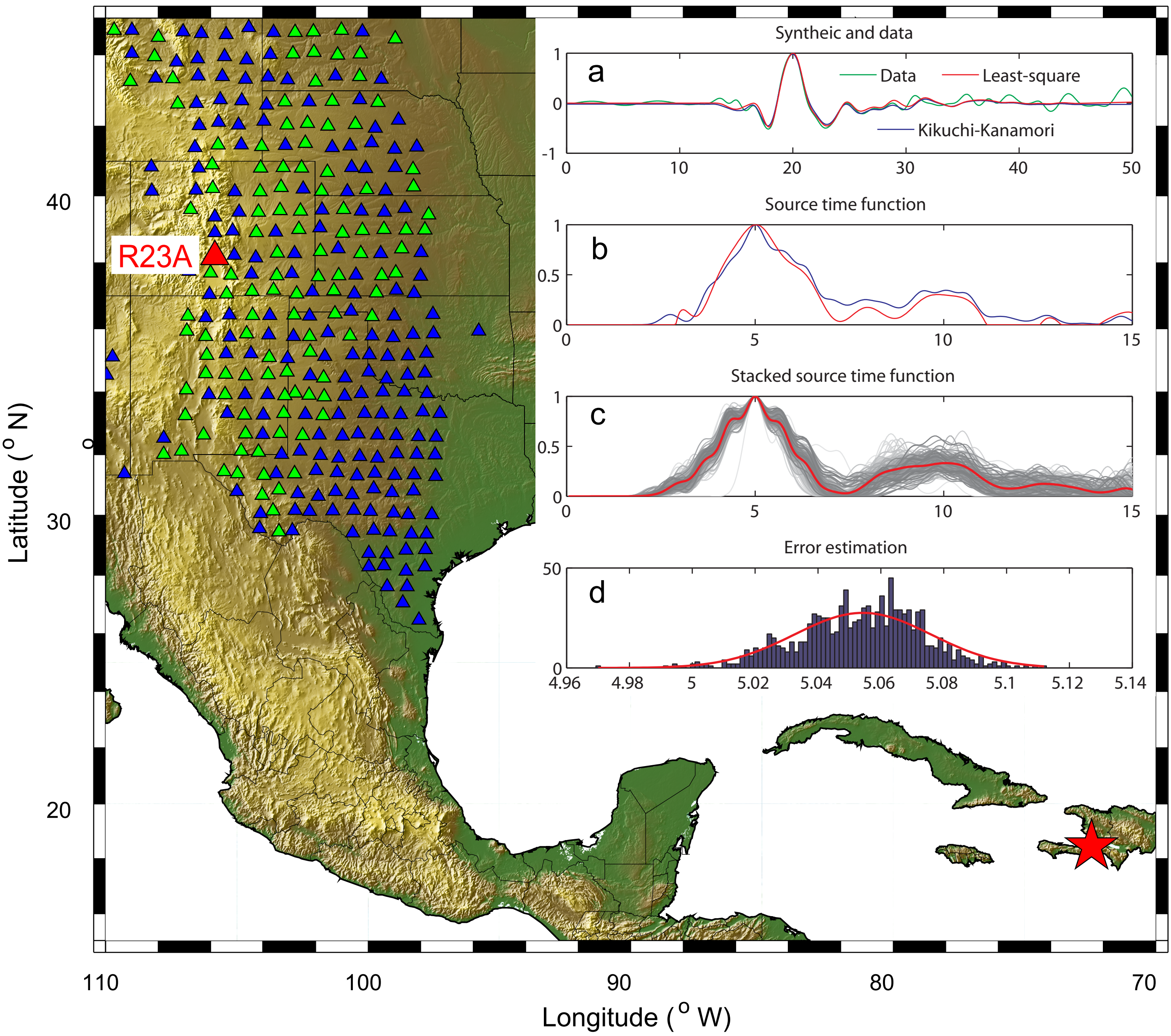

Syntheic and data
a
Data
Least-square
Kikuchi-Kanamori
Source time function
b
Stacked source time function
c
Error estimation
d
R23A
Latitude (o N)
Longitude (o W)
40
30
20
110
100
90
80
70

Kinematic model (InSAR+GPS+teleseismic)